Photodisintegration of ^{4}He into p+t

R. Nasseripour,[1] B.L. Berman,[1] N. Benmouna,[1, *] Y. Ilieva,[1, †] J.M. Laget,[2] K. P. Adhikari,[28] M.J. Amaryan,[28] M. Anghinolfi,[19] H. Baghdasaryan,[36] J. Ball,[9] M. Battaglieri,[19] I. Bedlinskiy,[22] A.S. Biselli,[13, 29] C. Bookwalter,[15] D. Branford,[12] W.J. Briscoe,[1] W.K. Brooks,[35, 2] V.D. Burkert,[2] S.L. Careccia,[28] D.S. Carman,[2] P.L. Cole,[17, 2] P. Collins,[4] P. Corvisiero,[19] A. D'Angelo,[20, 31] A. Daniel,[27] N. Dashyan,[38] R. De Vita,[19] E. De Sanctis,[18] A. Deur,[2] B Dey,[7] S. Dhamija,[14] R. Dickson,[7] C. Djalali,[33] G.E. Dodge,[28] D. Doughty,[10, 2] R. Dupre,[3] G. Fedotov,[32] S. Fegan,[16] R. Fersch,[37, ‡] A. Fradi,[21] M.Y. Gabrielyan,[14] G.P. Gilfoyle,[30] K.L. Giovanetti,[23] F.X. Girod,[9, §] J.T. Goetz,[5] W. Gohn,[11] E. Golovatch,[32, 19] R.W. Gothe,[33] K.A. Griffioen,[37] M. Guidal,[21] L. Guo,[2, ¶] H. Hakobyan,[35, 38] C. Hanretty,[15] N. Hassall,[16] D. Heddle,[10, 2] K. Hicks,[27] C.E. Hyde,[28] D.G. Ireland,[16] E.L. Isupov,[32] S.S. Jawalkar,[37] J.R. Johnstone,[16] K. Joo,[11, 2] D. Keller,[27] M. Khandaker,[26] P. Khetarpal,[29] A. Klein,[28] F.J. Klein,[8, 2] V. Kubarovsky,[2] S.E. Kuhn,[28] S.V. Kuleshov,[35, 22] V. Kuznetsov,[24, 9] K. Livingston,[16] H.Y. Lu,[33] M. Mayer,[28] M.E. McCracken,[7] B. McKinnon,[16] T Mineeva,[11] M. Mirazita,[18] V. Mokeev,[32, 2] K. Moriya,[7] B. Morrison,[4] E. Munevar,[1] P. Nadel-Turonski,[8] C.S. Nepali,[28] S. Niccolai,[21, 1] G. Niculescu,[23] I. Niculescu,[23, 1] M.R. Niroula,[28] M. Osipenko,[19] A.I. Ostrovidov,[15] K. Park,[33, 24, §] S. Park,[15] E. Pasyuk,[4] S. Anefalos Pereira,[18] S. Pisano,[21] O. Pogorelko,[22] S. Pozdniakov,[22] J.W. Price,[6] S. Procureur,[9] Y. Prok,[36, **] D. Protopopescu,[16] B.A. Raue,[14, 2] G. Ricco,[19] M. Ripani,[19] B.G. Ritchie,[4] G. Rosner,[16] P. Rossi,[18] F. Sabatié,[9] M.S. Saini,[15] J. Salamanca,[17] C. Salgado,[26] R.A. Schumacher,[7] H. Seraydaryan,[28] Y.G. Sharabian,[2, 38] D.I. Sober,[8] D. Sokhan,[12] S. Stepanyan,[2] P. Stoler,[29] S. Strauch,[33] R. Suleiman,[25] M. Taiuti,[19] D.J. Tedeschi,[33] S. Tkachenko,[28] M. Ungaro,[11] M.F. Vineyard,[34] D.P. Watts,[16, ††] L.B. Weinstein,[28] D.P. Weygand,[2] M. Williams,[7] E. Wolin,[2] M.H. Wood,[33] J. Zhang,[28] B. Zhao,[11, ‡‡] and Z.W. Zhao[33]

(The CLAS Collaboration)

[1] *The George Washington University, Washington, DC 20052*
[2] *Thomas Jefferson National Accelerator Facility, Newport News, Virginia 23606*
[3] *Argonne National Laboratory*
[4] *Arizona State University, Tempe, Arizona 85287-1504*
[5] *University of California at Los Angeles, Los Angeles, California 90095-1547*
[6] *California State University, Dominguez Hills, Carson, CA 90747*
[7] *Carnegie Mellon University, Pittsburgh, Pennsylvania 15213*
[8] *Catholic University of America, Washington, D.C. 20064*
[9] *CEA, Centre de Saclay, Irfu/Service de Physique Nucléaire, 91191 Gif-sur-Yvette, France*
[10] *Christopher Newport University, Newport News, Virginia 23606*
[11] *University of Connecticut, Storrs, Connecticut 06269*
[12] *Edinburgh University, Edinburgh EH9 3JZ, United Kingdom*
[13] *Fairfield University, Fairfield CT 06824*
[14] *Florida International University, Miami, Florida 33199*
[15] *Florida State University, Tallahassee, Florida 32306*
[16] *University of Glasgow, Glasgow G12 8QQ, United Kingdom*
[17] *Idaho State University, Pocatello, Idaho 83209*
[18] *INFN, Laboratori Nazionali di Frascati, 00044 Frascati, Italy*
[19] *INFN, Sezione di Genova, 16146 Genova, Italy*
[20] *INFN, Sezione di Roma Tor Vergata, 00133 Rome, Italy*
[21] *Institut de Physique Nucléaire ORSAY, Orsay, France*
[22] *Institute of Theoretical and Experimental Physics, Moscow, 117259, Russia*
[23] *James Madison University, Harrisonburg, Virginia 22807*
[24] *Kyungpook National University, Daegu 702-701, Republic of Korea*
[25] *Massachusetts Institute of Technology, Cambridge, Massachusetts 02139-4307*
[26] *Norfolk State University, Norfolk, Virginia 23504*
[27] *Ohio University, Athens, Ohio 45701*
[28] *Old Dominion University, Norfolk, Virginia 23529*
[29] *Rensselaer Polytechnic Institute, Troy, New York 12180-3590*
[30] *University of Richmond, Richmond, Virginia 23173*
[31] *Universita' di Roma Tor Vergata, 00133 Rome Italy*
[32] *Skobeltsyn Nuclear Physics Institute, Skobeltsyn Nuclear Physics Institute, 119899 Moscow, Russia*
[33] *University of South Carolina, Columbia, South Carolina 29208*
[34] *Union College, Schenectady, NY 12308*
[35] *Universidad Técnica Federico Santa María, Casilla 110-V Valparaíso, Chile*
[36] *University of Virginia, Charlottesville, Virginia 22901*
[37] *College of William and Mary, Williamsburg, Virginia 23187-8795*

^{38} *Yerevan Physics Institute, 375036 Yerevan, Armenia*

The two-body photodisintegration of ^{4}He into a proton and a triton has been studied using the CEBAF Large-Acceptance Spectrometer (CLAS) at Jefferson Laboratory. Real photons produced with the Hall-B bremsstrahlung-tagging system in the energy range from 0.35 to 1.55 GeV were incident on a liquid ^{4}He target. This is the first measurement of the photodisintegration of ^{4}He above 0.4 GeV. The differential cross sections for the γ^4He$\to pt$ reaction have been measured as a function of photon-beam energy and proton-scattering angle, and are compared with the latest model calculations by J.-M. Laget. At 0.6-1.2 GeV, our data are in good agreement only with the calculations that include three-body mechanisms, thus confirming their importance. These results reinforce the conclusion of our previous study of the three-body breakup of ^{3}He that demonstrated the great importance of three-body mechanisms in the energy region 0.5-0.8 GeV .

I. INTRODUCTION

One of the difficult challenges of nuclear physics is to understand the nature of the strong many-body interaction among the nucleons in the nucleus. In particular, understanding the contribution and manifestations of three-body forces is an important ingredient of the theoretical calculations that attempt to describe the reaction mechanisms. Photonuclear reactions are induced by a well known probe, and are especially sensitive to meson-exchange currents and isobar degrees of freedom.

The two-body photodisintegration of ^{4}He into a proton and a triton has been studied over the years in the low- and intermediate-energy regions, up to 0.4 GeV, where the one- and two-body mechanisms dominate the reaction [1, 2, 3, 4, 5]. The higher photon-energy region used in this experiment allows us to access larger momentum transfers, where the three-body mechanisms, mostly through higher-mass-meson double scattering, are expected to make a larger contribution.

In this analysis, the differential cross sections for the γ^4He $\to pt$ reaction were measured as a function of photon energy from 0.35 to 1.55 GeV, and over a wide range of the proton-scattering angle in the center-of-mass frame, as shown in Fig. 1. These measurements are complementary to the three-body breakup of ^{3}He for the study of three-body reaction mechanisms [6]. The re-

sults are compared with the latest model predictions of J.-M. Laget [7, 8], where three-body mechanisms for this channel are included in the calculations.
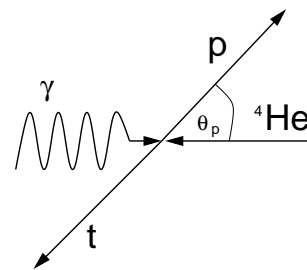

FIG. 1: Diagram of the γ^4He $\to pt$ reaction in the center-of-mass frame. The angle between the beam direction and the emitted proton in the center-of-mass frame is denoted as θ_p.
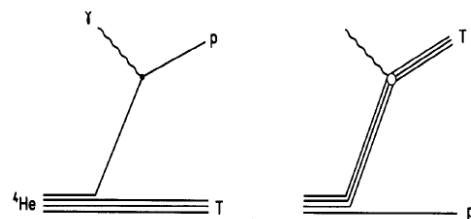
II. MODEL PREDICTIONS

FIG. 2: The one-body mechanisms included in the Laget model showing proton (left) and triton (right) exchange. This figure is from Ref. [7].

A calculation has been performed by J.-M. Laget [7] in which three types of reaction mechanisms for this channel have been included. Figures 2, 3, and 4 show the diagrams for one-body, two-body, and three-body reaction mechanisms, respectively. The one-body mechanisms include the proton and triton (three-nucleon) exchange di-

*Current address:Montgomery College, Rockville, MD 20850.

†Current address:University of South Carolina, Columbia, SC 29208.

‡Current address:University of Kentucky, LEXINGTON, KENTUCKY 40506

§Current address:Thomas Jefferson National Accelerator Facility, Newport News, Virginia 23606

¶Current address:Los Alamos National Laborotory, New Mexico, NM

**Current address:Christopher Newport University, Newport News, Virginia 23606

††Current address:Edinburgh University, Edinburgh EH9 3JZ, United Kingdom

‡‡Current address:College of William and Mary, Williamsburg, Virginia 23187-8795
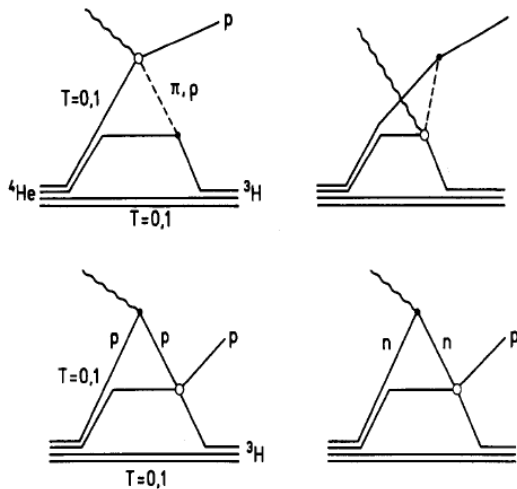
FIG. 3: The two-body mechanisms. The top diagrams show π and ρ exchange. The bottom diagrams show the nucleon-nucleon rescattering final-state interactions. The diagrams on the right come from the antisymmetry of the two active nucleons. This figure is from Ref. [7].
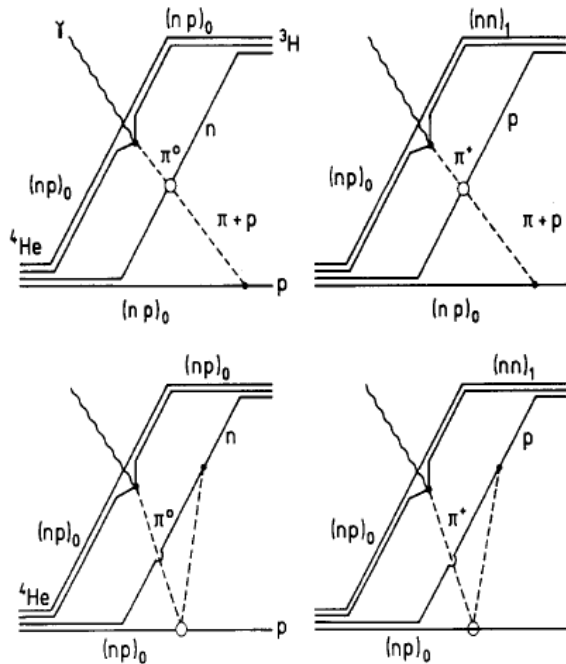

FIG. 4: The three-body mechanisms showing meson double scattering. The diagrams on the bottom correspond to the antisymmetry of the two nucleons in the pair that absorbs the intermediate pion. This figure is from Ref. [7].

agrams where a proton or a triton knockout is assumed. The proton-exchange diagram is dominant when the proton is emitted at forward angles. The two-body mechanisms included in this calculation are the two-nucleon meson exchange (including the pion and the rho meson) and nucleon-nucleon final-state interactions. The diagrams due to the antisymmetry of the two active nucleons are also included in the two-body mechanisms. The three-body mechanisms include the meson double-scattering amplitudes. As shown in the bottom panels of Fig. 4, diagrams that correspond to the antisymmetry of the two nucleons in the pair that absorbs the pion are also included in the model.

The two- and three-body diagrams included in this model were found to be dominant in the study of two- and three-body disintegration of ^{3}He. The relevance of this description is investigated here in a different environment, the ^{4}He nucleus, having markedly different n-body density and wave function.

Results of the model calculations are compared with previous world data in Fig. 5, where the cross sections are plotted as a function of the incident photon energy for three values of the proton angle with the incident photon-beam direction, $\theta_p = 60°$, $\theta_p = 90°$, and $\theta_p = 120°$. The comparison with Laget's model [7] reveals that three-body mechanisms must be taken into account to describe the data.

This model has been extended to higher energies according to Ref. [8] and improved using i) the full relativistic expression for the nucleon currents, ii) a high-energy diffractive NN scattering amplitude, and iii) the latest ground-state wave function [9] that has been generated from the Argonne AV18 NN potential [10] and the Urbana UIX three-nucleon force [11].

A thorough investigation of three-body mechanisms was performed earlier, in the analysis of the reaction $\gamma^3\text{He} \rightarrow ppn$ from the CLAS g3a data, which revealed that three-body mechanisms are most prominent in the energy range from 0.5 to 0.8 GeV [6]. Three-body mechanisms also have been studied in the two-body photodis-integration of ^{3}He [12]. The results presented here are the first to include the $\gamma^4\text{He} \rightarrow pt$ reaction at energies higher than 0.4 GeV.

III. EXPERIMENT AND DATA ANALYSIS

A. Experimental Apparatus

The $\gamma^4\text{He} \rightarrow pt$ reaction was measured during the g3a experiment in December 1999 with the CEBAF Large-Acceptance Spectrometer (CLAS) [13] at Jefferson Lab, shown in Fig. 6. CLAS is a large acceptance spectrometer used to detect multiparticle final states. Six superconducting coils generate a toroidal magnetic field around the target with azimuthal symmetry about the beam axis. The coils divide CLAS into six sectors, each functioning as an independent magnetic spectrom-
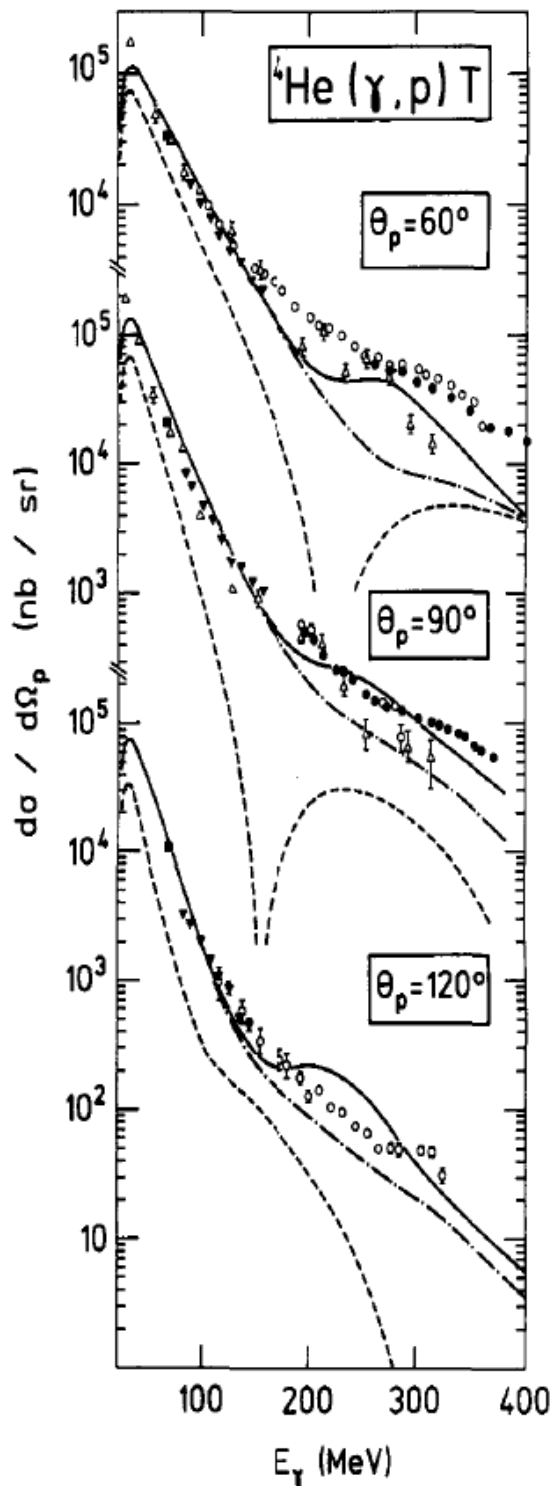
FIG. 5: Previous world data for the photodisintegration of ^{4}He into $p + t$, plotted as a function of the incident photon energy (open triangles [1], closed squares [2], closed circles [3], open circles [4], and closed diamonds [5]) compared with Laget's model calculations, including one-body diagrams only (dashed lines), two-body diagrams (dot-dashed lines), and three-body diagrams (solid lines). This figure is from Ref. [7].

eter. Each sector is instrumented with three regions of drift chambers (DCs), R1-3, to determine charged-particle trajectories [14], scintillator counters (SCs) for time-of-flight measurements [15], and, in the forward region, gas-filled threshold Cherenkov counters (CCs) for electron/pion separation up to 2.5 GeV [16], and electro-magnetic calorimeters (ECs) to identify and measure the energy of electrons and high-energy neutral particles, as well as to provide electron/pion separation above 2.5 GeV [17]. In the g3a experiment, real photons produced with the Jefferson Lab Hall-B bremsstrahlung-tagging system [18] in the energy range from 0.35 to 1.55 GeV were incident on an 18-cm-thick liquid ^{4}He target.

The photon beam was produced via bremsstrahlung from the primary electron beam operating at 1.645 GeV. Electrons were incident on the thin radiator of the Hall-B Photon Tagger [18]. Tagged photons were produced with 20-95% of the energy of the primary electron beam. About 10^9 triggers were collected at the production current of 10 nA. The magnetic field of CLAS toroidal magnet was set to 1920 A, half of its maximum value, to optimize the momentum resolution and the efficiency for positively charged particles. A trigger was used with a required coincidence between hits in the tagger, the start counter (ST), and the time-of-flight (TOF) paddles.

B. Event Selection

In order to associate the reaction of interest with the triggering tagged photon, the coincidence time between the Tagger and CLAS was required to be within 1 ns. A cut was applied to the time difference, Δt, between the CLAS start time at the interaction point recorded by the Start Counter (ST) and the Tagger. The central peak in Fig. 7 corresponds to the tagger hits that are in time coincidence with CLAS within the 2-ns-wide beam bucket. In the g3a run period, only about 2% of the events contained more than one tagged photon.

The particles were identified by determining their charge, momentum, and velocity. Charge and momentum were obtained from the drift-chamber tracking information and the velocity from the time of flight and path length to the time-of-flight detectors. Figure 8 shows the reconstructed mass distribution of positively charged particles. The events of interest were those with two and only two positively charged particles detected in coincidence. A triton candidate was required to have a positive charge and a reconstructed mass squared m^2 between 6.5 and 11.0 $(\text{GeV}/c^2)^2$. A proton candidate was required to have a positive charge and a reconstructed mass squared between 0.4 and 1.4 $(\text{GeV}/c^2)^2$. In order to assure that the events of interest are produced within the ^{4}He target volume, a cut was applied to the z-component of the interaction vertex along the beam line.

Energy-loss corrections were applied to the selected particles because they lose a non-negligible part of their energy in the target material and start counter before
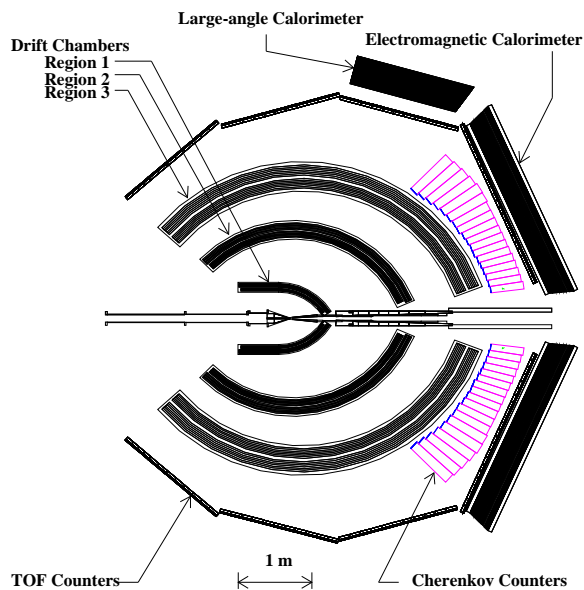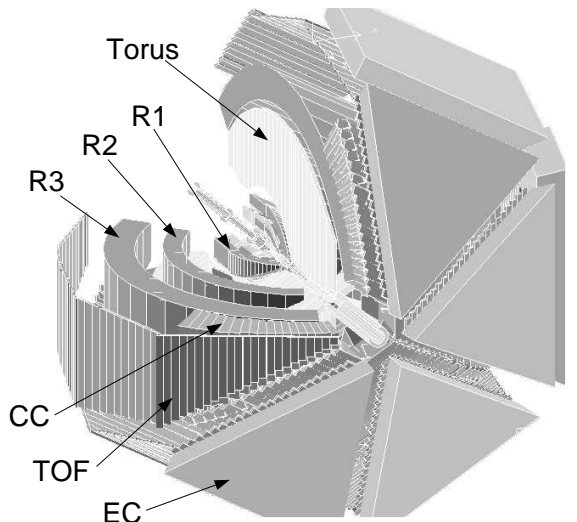
FIG. 6: CLAS is a nearly 4π-sr detector system used to observe multiparticle final states. Top: Three-dimensional representation of CLAS, with a portion of the system cut away to highlight elements of the detector system as described in the text. Bottom: Midplane slice of the CLAS.
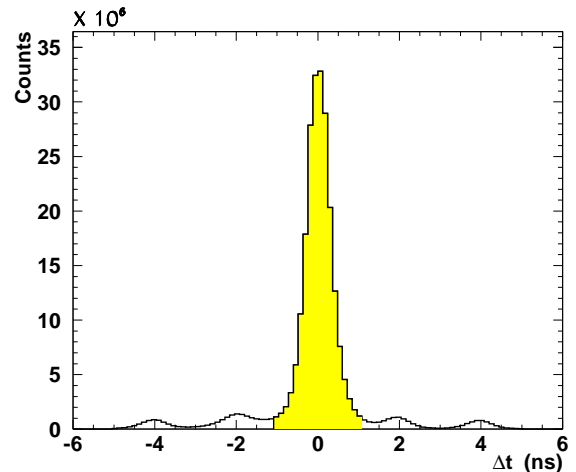

FIG. 7: (Color online) Difference between tagger and the start-counter (ST) times (solid histogram). The tagger and ST coincidence time for the selected events is required to be within 1 ns (shaded histogram). Secondary peaks corresponding to nearby beam buckets are also visible.

the measurement of the triton than of the proton. Table I summarizes the result of fitting Gaussians to the proton and triton missing-mass-squared distributions before and after the energy-loss corrections.

Also, fiducial-volume cuts were applied to ensure that the particles are detected within those parts of the volume of CLAS where the detection efficiency is high and uniform. These cuts select regions of the CLAS where simulations reproduce detector response reasonably well.

In order to eliminate any possible background, two-body kinematics were used to select a clean sample of pt events (see Sec. III C). .

TABLE I: Summary of the obtained mean values and widths of the proton and triton missing-mass-squared distributions before and after the energy-loss corrections. The accepted values for the proton and triton mass squared are 0.8804 and 7.890 $(\text{GeV}/c^2)^2$, respectively.

	without corrections	with corrections
MM^2_p $(\text{GeV}/c^2)^2$	7.919	7.883
Width $(\text{GeV}/c^2)^2$	0.09238	0.09127
MM^2_t $(\text{GeV}/c^2)^2$	1.100	0.8879
Width $(\text{GeV}/c^2)^2$	0.1001	0.06159

they reach the drift chambers. The effect of the energy-loss corrections after applying all of the kinematic cuts on the final sample of pt data is shown in Fig. 9. The importance of these corrections can be demonstrated by comparing the missing-mass squared of either the detected proton or the detected triton before and after applying these corrections. As expected, the amount of the energy loss for a particle depends on the mass of that particle and, therefore, these corrections have a larger effect on

C. Background Corrections

In order to select cleanly the $\gamma^4\text{He} \to pt$ channel, two-body kinematics were used. The two-body final-state kinematics for real events requires that the missing energy, missing momentum, and missing-mass squared for pt events be zero. Also, the opening angle between the
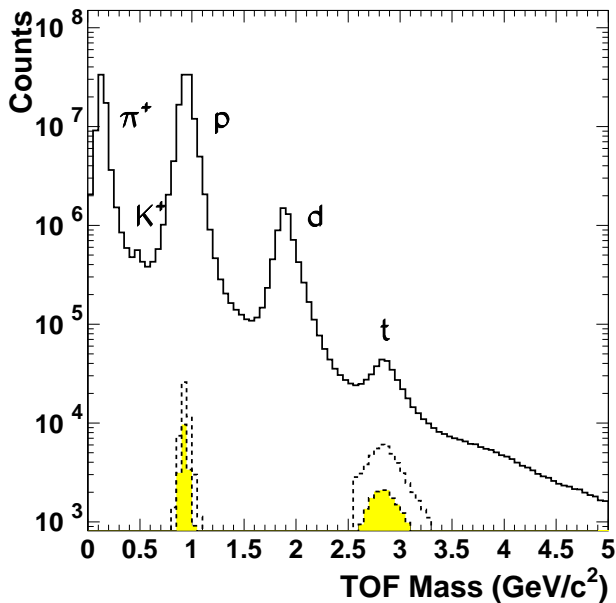
FIG. 8: (Color online) Hadron mass calculated from the time-of-flight and tracking information. The solid histogram shows the mass distribution for all of the positively charged hadrons, the dashed histogram is the selected sample of protons and tritons that are detected in coincidence, and the shaded histogram shows the same distribution after applying all of the kinematic cuts to remove the background (see Sec. III C for details).
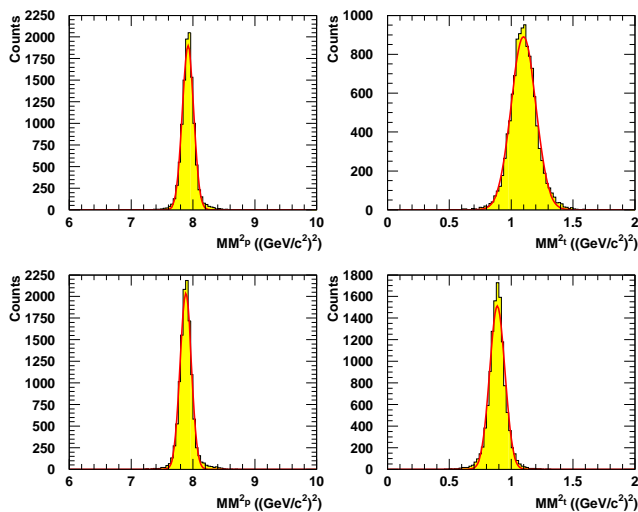

FIG. 9: (Color online) Distributions of the proton (left) and triton (right) missing-mass squared before (top) and after (bottom) the energy-loss corrections. Gaussian fits have been performed to determine the mean value and the width of each distribution (see Table I).

three-vectors of the detected proton and triton θ_{pt} should be close to $180°$ in the center-of-mass frame. Our initial sample of events contains two and only two charged particles. Four-vector conservation for the reaction γ^4He $\to pt$, as specified in Eq.(1), leads to the determination of three kinematic variables – the missing energy E_X, the missing momentum $P_X = \sqrt{P_X(x)^2 + P_X(y)^2 + P_X(z)^2}$, and the missing-mass squared $M_X^2 = E_X^2 - P_X^2$:

$$\begin{pmatrix} E_\gamma \\ 0 \\ 0 \\ E_\gamma \end{pmatrix} + \begin{pmatrix} M_{4He} \\ 0 \\ 0 \\ 0 \end{pmatrix} =$$

$$\begin{pmatrix} \sqrt{m_p^2 + p_p^2} \\ p_p(x) \\ p_p(y) \\ p_p(z) \end{pmatrix} + \begin{pmatrix} \sqrt{m_t^2 + p_t^2} \\ p_t(x) \\ p_t(y) \\ p_t(z) \end{pmatrix} + \begin{pmatrix} E_X \\ P_X(x) \\ P_X(y) \\ P_X(z) \end{pmatrix}, \quad (1)$$

where E_γ is the incident photon energy, M_{4He} is the mass of the target nucleus, m_p and m_t are the masses of the proton and triton, respectively, and p_p and p_t are the measured three-momenta of the proton and triton, respectively. These kinematic variables are plotted in Fig. 10. For the real two-body break-up events into pt, we then have $E_X = 0$ GeV, $P_X = 0$ GeV/c, $M_X^2 = 0$ $(\text{GeV}/c^2)^2$, and $\theta_{pt} = 180°$. Indeed, in Fig. 10 we see clear peaks showing the real two-body pt break-up events. However, some background can be seen in the selected events. These events (mostly due to the $pt\pi^0$ channel) can be removed by applying additional kinematic cuts as follows:

1. The first cut is applied to the difference between the measured scattering angle of the proton in the center-of-mass frame (from the measured three-momentum vector of the proton) and the calculated one from the conservation of the four-momenta in the γ^4He $\to pt$ reaction (by measuring only the triton momentum). This difference is plotted in the upper-left side of Fig. 11. The clear peak around zero corresponds to the real events from the two-body breakup of ^{4}He into a proton and triton. The events for which this angular difference is outside of the range [-0.15,0.15] were removed from the data.

2. The second cut is applied to the difference between the momenta of the proton and the triton in the center-of-mass frame. For the real pt events, this difference shows a peak around zero with a tail that could be due to the $pt\pi^0$ events, as shown in the upper-right panel of Fig. 11. The applied cut requires this difference to be between -0.15 and 0.15 GeV/c.

3. The third cut requires the proton and triton three-momenta to be in the same plane, i.e., the difference between the azimuthal angles for the proton
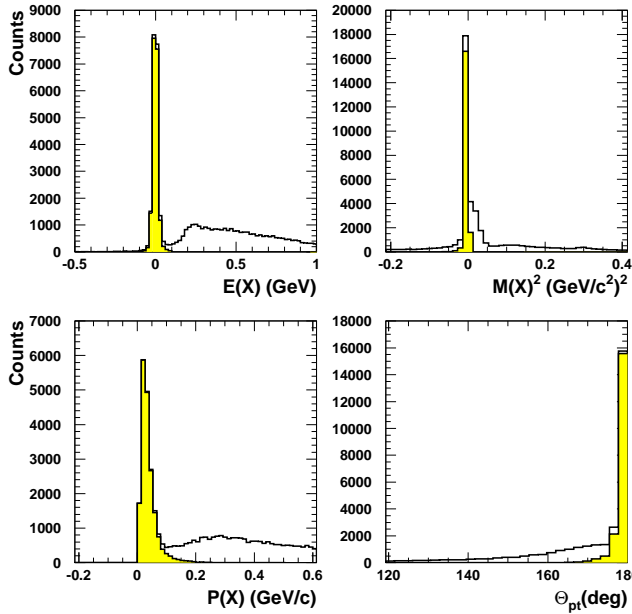
FIG. 10: (Color online) The pt two-body final-state kinematics require the missing energy (upper left), missing-mass squared (upper right), and missing momentum (lower left) to be zero, and the pt opening angle in the center-of-mass frame (lower right) to be 180°. The peaks correspond to the real pt events from the two-body breakup of ^{4}He. The shaded areas correspond to the nearly background-free sample of pt events after the kinematic cuts described in this section were applied. The upper left panel shows the cut applied to the missing energy for pt events; the other three panels show the derived event distributions.
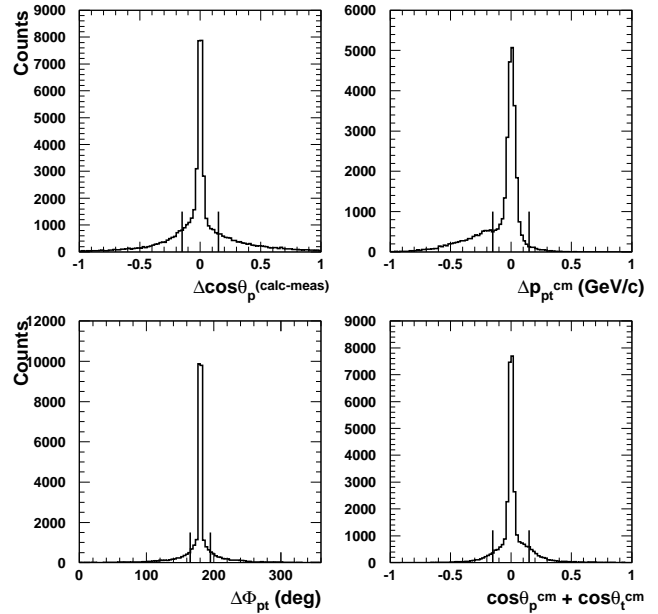

FIG. 11: Cuts were applied on various kinematic variables to remove the background. Upper left: The difference between the measured and calculated proton scattering angles. Upper right: The difference between the magnitude of proton and triton momenta. Lower left: The difference between the proton and triton azimuthal angles. Lower right: The sum of the cosines of the proton and triton scattering angles. All quantities are shown in the center-of-mass frame.

and the triton in the center-of-mass frame is selected to be $165° < \phi_{pt}^{cm} < 195°$. This distribution is shown in the lower-left panel of Fig. 11. A prominent peak around 180° is clearly seen.

4. The fourth cut is applied to the sum of the cosines of the proton and triton scattering angles in the center-of-mass frame, shown in the lower-right panel of Fig. 11. This cut retains only those events with $-0.15 < \cos\theta_p^{cm} + \cos\theta_t^{cm} < 0.15$.

5. Finally, the fifth cut requires the pt missing energy to be $-0.1 < E(X) < 0.1$ GeV, shown in the upper left panel of Fig. 10.

The value of each of these cuts is optimized such that the maximum number of "good" pt events is retained. Using these cuts, the background in the spectra of the previously described kinematic variables is mostly removed, as can be seen for the shaded areas of Fig. 10. The sample of events used after these cuts is therefore essentially background-free. This also can be confirmed by calculating the missing-mass squared of either the detected proton or the detected triton. These distributions are shown before and after the above cuts in Fig. 12, and
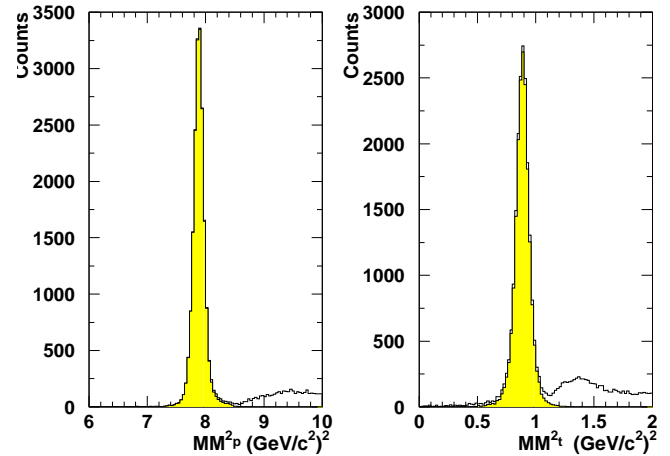

FIG. 12: (Color online) The calculated values for the missing-mass squared for the detected proton (left) and the detected triton (right), before (solid histogram) and after (shaded histogram) applying the kinematic cuts. The background is completely removed by the kinematic cuts (see Sec. III C for details).

show that the background has been completely removed. The clean sample of protons and tritons that are detected in coincidence is also shown within the shaded areas of Fig. 8.

Table II summarizes the final cuts used to identify the pt events as described in this section.

TABLE II: Summary of kinematic cuts for event selection.

Description	Cut
Coincidence time Δt	< 1 nsec
Positively charged particles	2
Proton identification	$0.4 < m_p^2 < 1.4$ (GeV/c^2)^2
Triton identification	$6.5 < m_t^2 < 11.0$ (GeV/c^2)^2
z-vertex	[-8,8] (cm)
$\Delta \cos \theta_p^{cm}$	[-0.15,0.15]
$\Delta p_{p,t}^{cm}$	[-0.15,0.15] (GeV/c)
$\Delta \phi_{p,t}^{cm}$	[165,195] deg
$\cos \theta_p^{cm} + \cos \theta_t^{cm}$	[-0.15,0.15]

D. Detector Efficiency and Acceptance

The raw pt yields are obtained as a function of the photon beam energy E_γ and the proton polar angle in the center-of-mass frame θ_p^{cm}. The yields are corrected for the detector acceptance using a Monte-Carlo simulation of phase-space-distributed pt events within the entire 4π solid angle. The photon energy was generated randomly with a uniform distribution from 0.35 to 1.55 GeV. The standard GEANT-based CLAS simulation package [19]) was used to simulate the detector response. The simulated events were processed with the same event-reconstruction software that was used to reconstruct the real data. Figure 13 shows the reconstructed mass distributions for the simulated events with one proton and one triton after applying all of the cuts.

The acceptance is defined as the ratio of the number of reconstructed events to the number of generated events. Owing to the geometry and the structure of CLAS, there are regions of solid angle that are not covered by the detector. Furthermore, the inefficiencies in the various components of the detector affect its acceptance and consequently the event reconstruction in CLAS. The acceptance correction factors are shown as functions of proton scattering angle θ_p^{cm} and photon energy E_γ for each kinematic bin in Fig. 14. These correction factors are used to convert the raw yields into unnormalized cross sections. Data points with poor acceptance (< 0.4) at smaller angles are not included in the final data set.
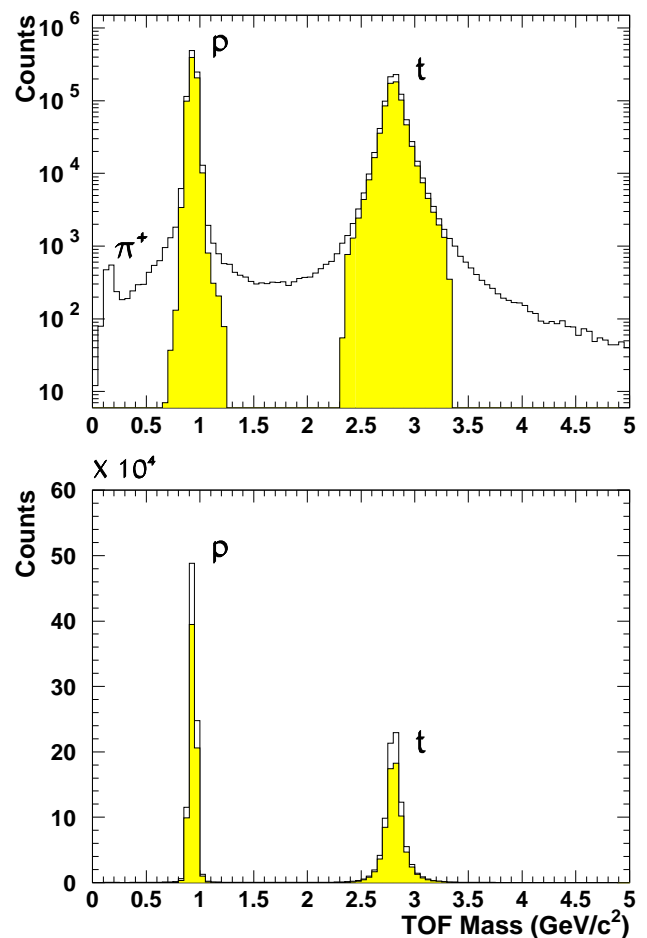

FIG. 13: (Color online) Simulated TOF masses for Monte-Carlo generated events, plotted with both logarithmic (top) and linear (bottom) scales, before (solid histogram) and after (shaded areas) applying all of the cuts.

IV. RESULTS

A. Cross Sections

The differential cross sections are obtained from the expression

$$\frac{d\sigma}{d\Omega} = \frac{N}{\eta_a N_\gamma N_T \Delta\Omega} \tag{2}$$

where N is the number of measured events in a given energy and angular bin of solid angle $\Delta\Omega = 2\pi \Delta \cos\theta_{cm}$. The CLAS acceptance is given by η_a; N_γ is the number of photons within the given energy range incident on the target; and N_T is the number of target nuclei per unit area.

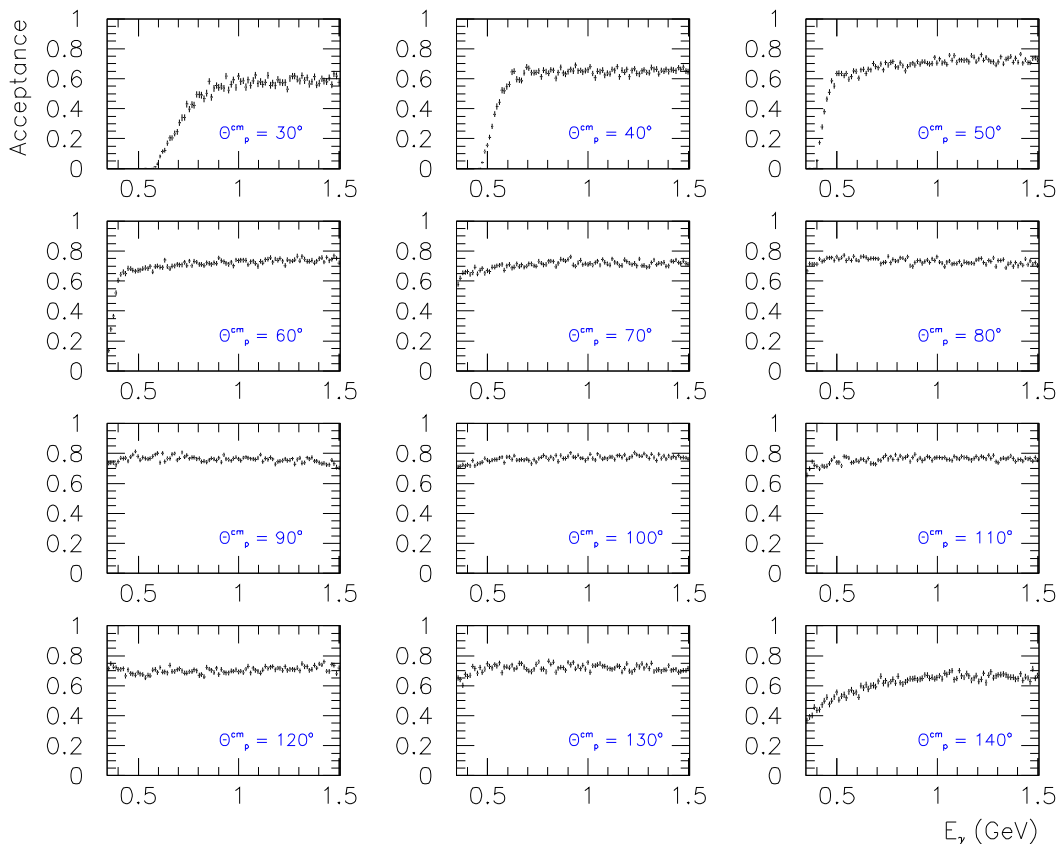The number of target nuclei per unit area N_T is determined from

FIG. 14: (Color online) Acceptance as a function of photon energy E_γ for various proton-scattering-angle bins.

$$N_T = \frac{\rho l N_A}{A} \approx 3.0066 \times 10^{-10} \ \text{nb}^{-1}, \qquad (3)$$

where $l = 16.0$ cm is the target length, $\rho = 0.1249$ g/cm^3 is the density of liquid ^{4}He, $A = 4.0026$ g/mole is its atomic weight, and $N_A = 6.022 \times 10^{23}$ atoms/mole is Avogadro's number.

The photon yield N_γ was obtained from the Tagger hits using the gflux analysis package [20]. This number is corrected for the data-acquisition dead time. The angle-integrated cross section as a function of photon energy is shown in Fig. 15 in linear and logarithmic scales. The logarithmic plot was fitted with an Ae^{-BE_γ} functional form with $A = 1.35$ μb, and $B = 7.8$ GeV^{-1}. It is remarkable that the total cross section follows an exponential fall-off so closely, over the entire energy range from 0.4 to $\sim$1.0 GeV, flattening somewhat only above this energy, where forward angles dominate.

The measured differential cross sections are shown in Figs. 16 and 17 as functions of photon energy and proton-scattering angles, respectively. These plots show that the peak of the angular distributions shifts slightly towards smaller angles with increasing photon energy.

B. Systematic Uncertainties

Table III summarizes the systematic uncertainties. The uncertainty in the photon-flux determination, including the tagger-efficiency evaluation, is taken from the g3a analysis of Niccolai *et al.* [6]. The value of the target density given in the literature was used; its uncertainty is no larger than 2%. The uncertainties due to the fiducial cuts are estimated and have been found to be negligible. The systematic uncertainty due to the CLAS acceptance

TABLE III: Summary of systematic uncertainties arising from various sources.

Source	Uncertainty (%)
Photon flux	6
Target density	< 2
Solid angle	negligible
CLAS acceptance	< 10
Fiducial cuts	negligible
Kinematic cuts	< 10
Total	< 15

was obtained by comparing the cross sections measured by each pair of the CLAS sectors independently (i.e., the data from sectors 1 and 4, 2 and 5, and 3 and 6 were
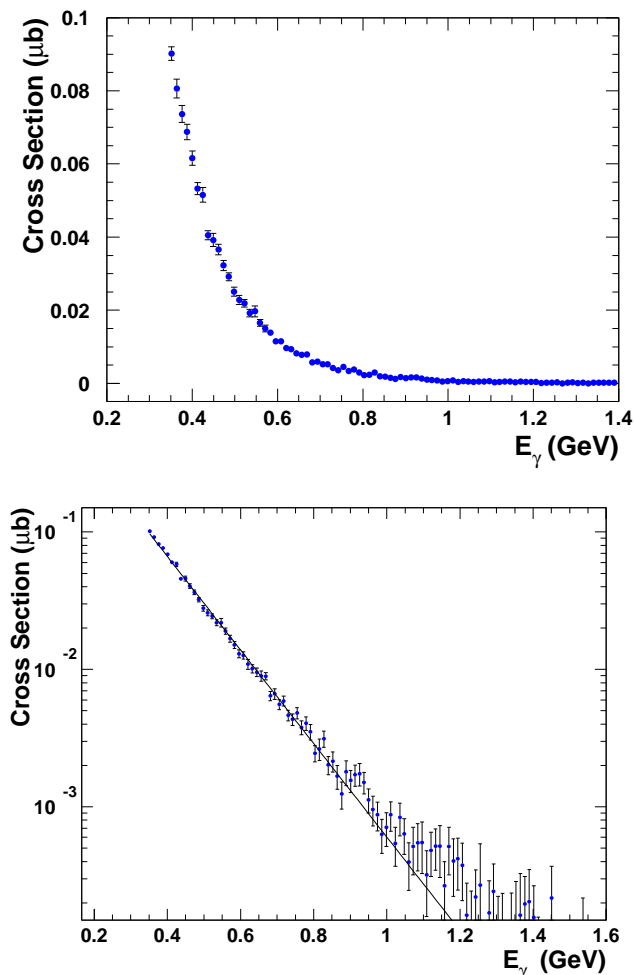
FIG. 15: (Color online) Total angle-integrated cross section as a function of E_γ in linear (top) and logarithmic (bottom) scales. Error bars indicate statistical uncertainties. The logarithmic plot was fitted with an Ae^{-BE_γ} functional form with $A =$ 1.35 μb, and $b =$ 7.8 GeV^{-1}.

combined). The mean deviation between the three sets of cross sections is considered to be an estimate of the systematic uncertainty for the CLAS acceptance.

In order to estimate the systematic uncertainty due to applying the kinematic cuts, two sets of altered cuts, loose and tight, were used and compared with the nominal cuts. The RMS (root mean square) of the distribution of the differences between the cross sections obtained with loose, tight, and the nominal cuts is considered to be a measure of the systematic uncertainty due to these cuts.

The CLAS acceptance and kinematic cuts contribute the largest part of the systematic uncertainty. The individual systematic uncertainties are summed in quadrature to less than 15%. The statistical uncertainties for the results usually dominate the systematic uncertainties.
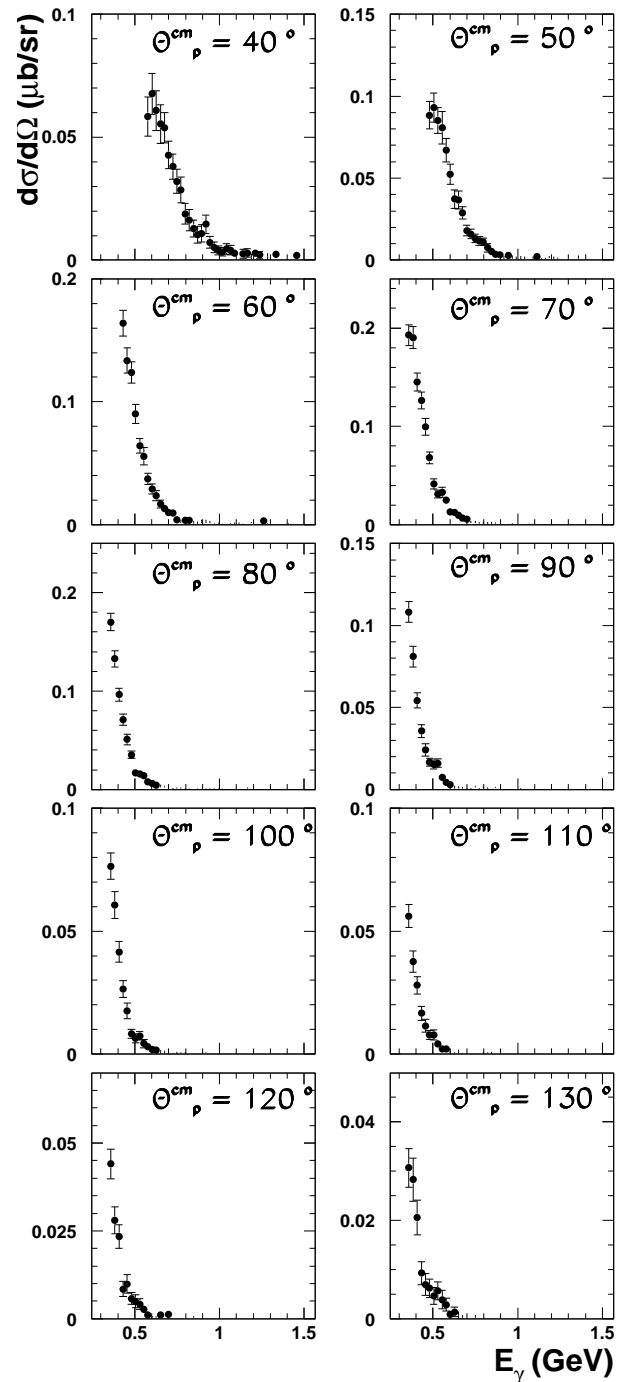

FIG. 16: Measured differential cross sections as a function of E_γ for $\theta_p^{cm} =$ 40, 50, 60, 70, 80, 90, 100, 110, 120, and 130 degrees. Error bars indicate statistical uncertainties.

V. DISCUSSION AND SUMMARY

Our bin-averaged cross sections are compared in Figs. 18 and 19 with the latest model calculations by J.-M. Laget [8]. Figure 18 shows the cross sections as a function
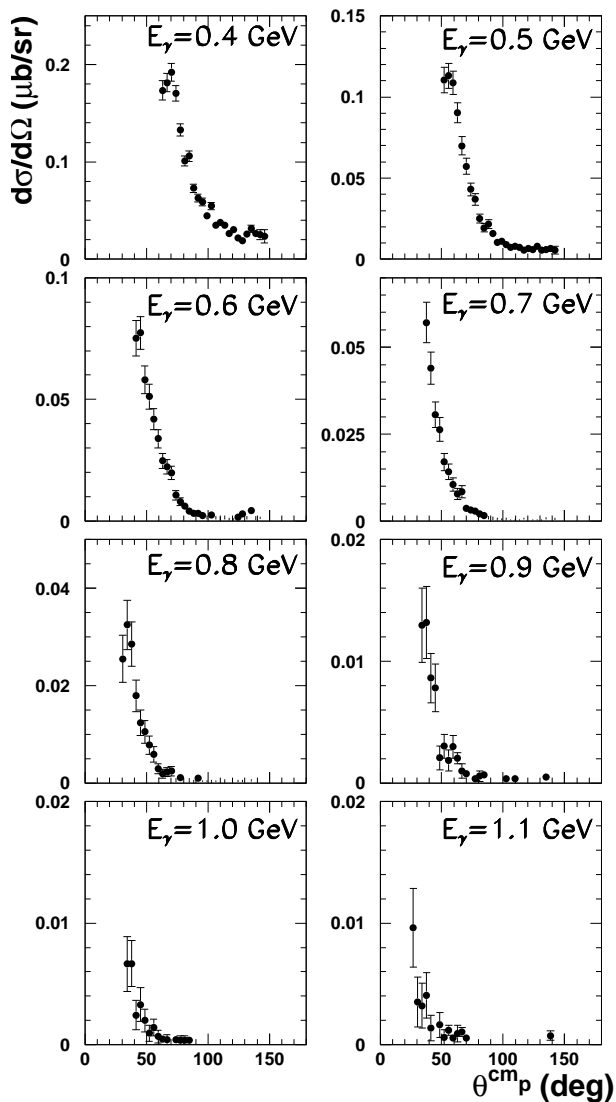
FIG. 17: Measured differential cross sections as a function of θ_p^{cm} for E_γ = 0.4, 0.5, 0.6, 0.7, 0.8, 0.9, 1.0, and 1.1 GeV. Error bars indicate statistical uncertainties.

FIG. 18: (Color online) Measured differential cross sections compared with the Laget calculations [8]. The results are shown as a function of θ_p^{cm} for four photon-energy bins. The curves are calculations based on the Laget model [7] including one-body (dashed line), two-body (dash dotted line), and three-body (solid red line) mechanisms. Error bars indicate statistical uncertainties.

of proton-scattering angle in the center-of-mass frame for four energy bins, centered at 0.6, 0.8, 1.0, and 1.2 GeV. Each energy bin is 100 MeV wide.

In general, for all photon-energy bins, our data are in qualitative agreement only with the calculations that include three-body mechanisms, confirming the importance of the contribution of three-body mechanisms at these energies. At 0.6 and 0.8 GeV, our data are higher than the calculations between 60 and 100 degrees, and between 60 and 80 degrees, respectively. Our data are consistent with the three-body calculations at large angles for all photon-energy bins. However, at the higher of these energies, and at small proton angles, there are discrepancies between the data and the results of the cal-
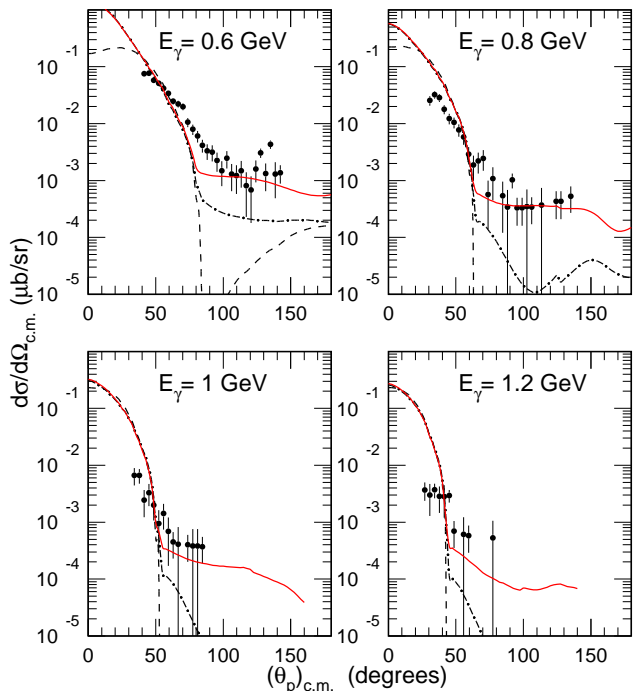
culations. This disagreement at the most forward angles at higher energies might result from either of two factors: 1) Off-mass-shell effects might become significant when the energy increases. Although the elementary electromagnetic operator (the coupling of the photon to the nucleon) used in this model is the fully relativistic version of the coupling of the photon to an on-mass-shell nucleon, the actual photon energy that enters the amplitude is not the same as the photon energy when the target proton is at rest. The difference between the two energies increases with the photon energy. This is a well identified problem that still has no definite solution. 2) The previous drawback is less severe for the three-body amplitude that dominates at large angles. Here, the momentum transfer is shared between the three nucleons and one probes mainly the low-momentum components of the ^{4}He wave function. Also, the amplitude depends mainly on the elementary processes, where the nucleons are mostly on-shell.

The cross sections are shown in Fig. 19 as a function of photon energy for three angular bins centered at 60, 90, and 120 degrees. Each angular bin is 10 degrees wide. Comparison with Fig. 5 shows that the trend of the data and calculations are very similar. However there
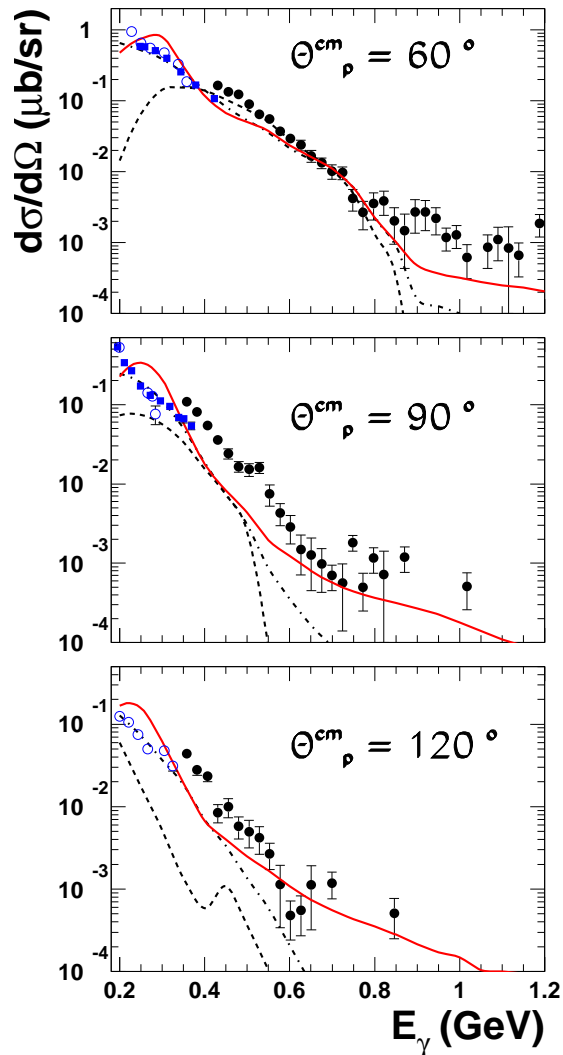
FIG. 19: (Color online) Measured differential cross sections (closed circles) compared with the data from Ref. [2] (closed squares), Ref. [4] (open blue circles), and the Laget calculations [8], as a function of photon energy for three proton center-of-mass angles. The curves are as described in Fig. 18. Error bars indicate statistical uncertainties.

is a clear difference between the relative strength of the two- and three-body contributions with respect to the one-body contribution shown in the two plots. This is because the earlier version of the Laget model [7] used the AV14 potential [21]. This version included fewer high-momentum components than the newer version, which uses AV18 [10]. Comparison shows that in general our data stand above all the curves especially at 90 and 120 degrees but qualitatively are in good agreement with the calculations.

Figure 19 also shows some of the earlier experimental data from the Saclay group [2] and the MIT group [3], compared with the results of this experiment. There is a very limited overlap in the photon energy range between our data and the older data from Saclay. The range of the overlap is from 423 to 430 MeV for 60 degrees, and from 357 to 369 for 90 degrees. There is no overlap at all between our data and older data from MIT. The comparison shows a continuous trend with increasing photon energy for the previous data to lie below our data in the overlap region.

In summary, we have measured the differential cross sections for the $\gamma^4\text{He} \rightarrow pt$ reaction in the energy range from 0.35 to 1.55 GeV, for proton center-of-mass scattering angles between 40 and 140 degrees. It is important to emphasize that the interpretation of these data is model dependent. We have compared them with the results of the only available theoretical calculation at these energies [8]. This comparison reveals the essential importance of the contribution of three-body mechanisms, especially in the energy region of 0.6-0.8 GeV, as was found previously for ^3He [6]. These data are important for understanding the reaction mechanisms and for developing models of this process for photon energies above 0.4 GeV, and even more important for an understanding and appreciation of the importance, in the relevant range of energy and wavelength, of strong many-body forces in nuclei.

Acknowledgments

[1] S.E. Kiergan, A.O. Hanson, and L.J. Koester, Phys. Rev. C **8**, 431 (1973).

[2] P.E. Argan *et al.*, Nucl. Phys. **A 237**, 447 (1975).

[3] J. Arends *et al.*, Nucl. Phys. **A 322**, 253 (1979).

[4] R.A. Schumacher *et al.*, Phys. Rev. C **33**, 50 (1986).

[5] R.T. Jones *et al.*, Phys. Rev. C **43**, 2052 (1991).

[6] S. Niccolai *et al.* (CLAS Collaboration), Phys. Rev. C **70**, 064003 (2004).

[7] J.-M. Laget, Nucl. Phys. **A 579**, 333 (1994).

[8] J.-M. Laget, Phys. Lett. **B 609**, 49 (2005), and private communication (2009).

[9] J. Forest *et al.*, Phys. Rev. C **54**, 646 (1996).

[10] R. B. Wiringa *et al.*, Phys. Rev. C **51**, 38 (1995).

[11] B. S. Pudliner *et al.*, Phys. Rev. Lett. **74**, 4396 (1995).

[12] J.-M. Laget, Phys. Rev. C **38**(R), 29993 (1988).

[13] B.A. Mecking *et al.* (CLAS Collaboration), Nucl. Instrum. Methods **A 503**, 513 (2003).

[14] M. D. Mestayer *et al.*, Nucl. Instrum. Methods **A 449**, 81 (2000).

[15] E. S. Smith *et al.*, Nucl. Instrum. Methods **A 432**, 265 (1999).

[16] G. Adams *et al.*, Nucl. Instrum. Methods **A 465**, 414 (2001).

[17] M. Amarian *et al.*, Nucl. Instrum. Methods **A 460**, 239 (2001).

[18] D.I. Sober *et al.*, Nucl. Instrum. Methods **A 440**, 263 (2000).

[19] CLAS GEANT Simulation, http://www.physics.unh.edu/maurik/Gsim/

[20] J. Ball and E. Pasyuk, CLAS-NOTE 2005-002 (2005).

[21] R. B. Wiringa *et al.*, Phys. Rev. C **29**, 1207 (1984).